Perovskite Oxide SrTiO3 as an Efficient Electron Transporter for Hybrid Perovskite Solar Cells

6 AUTHORS, INCLUDING:

Ashok Bera
King Abdullah University of Science and Techn…
19 PUBLICATIONS   483 CITATIONS

SEE PROFILE

Erkki Alarousu
King Abdullah University of Science and Techn…
71 PUBLICATIONS   498 CITATIONS

SEE PROFILE

Omar F Mohammed
King Abdullah University of Science and Techn…
89 PUBLICATIONS   1,226 CITATIONS

SEE PROFILE

Tom Wu
King Abdullah University of Science and Techn…
225 PUBLICATIONS   4,960 CITATIONS

SEE PROFILE

Perovskite Oxide SrTiO₃ as an Efficient Electron Transporter for Hybrid Perovskite Solar Cells

Ashok Bera,[†] Kewei Wu,[†] Arif Sheikh,[†] Erkki Alarousu,[‡] Omar F. Mohammed,*[,‡] and Tom Wu*[,†]

[†]Materials Science and Engineering, King Abdullah University of Science and Technology (KAUST), Thuwal 23955-6900, Saudi Arabia

[‡]Solar and Photovoltaics Engineering Research Center, Physical Sciences and Engineering Division, King Abdullah University of Science and Technology (KAUST), Thuwal 23955-6900, Saudi Arabia

🅢 Supporting Information

ABSTRACT: In this work, we explored perovskite oxide SrTiO₃ (STO) for the first time as the electron-transporting layer in organolead trihalide perovskite solar cells. The steady-state photoluminescence (PL) quenching and transient absorption experiments revealed efficient photoelectron transfer from CH₃NH₃PbI₃₋ₓClₓ to STO. Perovskite solar cells with *meso*-STO exhibit an open circuit voltage of 1.01 V, which is 25% higher than the value of 0.81 V achieved in the control device with the conventional *meso*-TiO₂. In addition, an increase of 17% in the fill factor was achieved by tailoring the thickness of the *meso*-STO layer. We found that the application of STO leads to uniform perovskite layers with large grains and complete surface coverage, leading to a high shunt resistance and improved performance. These findings suggest STO as a competitive candidate as electron transport material in organometal perovskite solar cells.
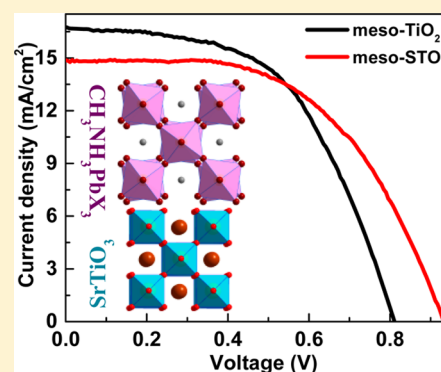
1. INTRODUCTION

Highly efficient solid-state sensitized photovoltaic technology is emerging as a promising and cost-effective contender for harvesting solar power as a renewable source of energy. Recently, organic−inorganic hybrid perovskites, CH₃NH₃PbX₃ (X is iodine or a mixture of iodine and chlorine), have been intensively pursued as solid-state sensitizers.[1−17] This class of materials possesses several advantages, such as a direct band gap of ∼1.55 eV, high absorption coefficient,[10] high electron mobility,[18] and solution processability.[19] In a typical perovskite solar cell, the absorber layer with a thickness of several hundred nanometers is sandwiched between the electron-transporting layer (ETL) and the hole-transporting layers (HTLs). Under light illumination, the photogenerated charge carriers in the perovskite absorber are quickly injected into the ETL and HTL and subsequently collected as a photocurrent through the top and bottom electrodes. Halide perovskites are good light absorbers and capable of generating a high photocurrent. However, similar to dye-sensitized solar cells (DSSCs),[20,21] perovskite solar cells with mesoscopic ETLs suffer from a loss in open-circuit voltage (V_{OC}), which compromises the overall efficiency. One direct approach to improving V_{OC} in solid-state sensitized solar cells is to reduce the band offset between the sensitizer and the ETL/HTL.

In mesoscopic perovskite solar cells, CH₃NH₃PbX₃ sensitizers are usually deposited on mesoporous TiO₂ by either one-step spin-coating or two-step spin-coating/dip-coating techniques followed by a solid-state HTL of 2,2′,7,7′-tetrakis(*N*,*N*-di-*p*-methoxyphenylamine)-9,9′-spirobifluorene (spiro-MeO-TAD). With one-step spin-coating of the CH₃NH₃PbI₃₋ₓClₓ sensitizer between the mp-TiO₂ ETL and the spiro-MeOTAD HTL, the average V_{OC} was found to be ∼0.80 V.[5,15,22,23] With an additional processing step, the two-step methods generally can lead to better morphology and crystalline quality of the perovskite layer as well as higher V_{OC}.[2,24,25] It is noteworthy that most efforts of improving V_{OC} have been focusing on the HTL, while *meso*-TiO₂ remains as the dominating choice of ETL. By engineering the band alignment between the trihalide perovskites and the HTL, V_{OC} of >1 V has been reported recently.[26,27] For mixed-halide perovskite CH₃NH₃PbI₃₋ₓClₓ solar cells, a high V_{OC} has been reported by replacing the electron-transporting *meso*-TiO₂ layer with *meso*-Al₂O₃ scaffold.[12] However, Al₂O₃ is a highly insulating material, and the improvement of the solar cell performance should be attributed to the better structural and transport properties of the perovskite. A similar improvement of perovskite absorption and coverage was recently achieved by adding CH₃NH₃Cl to the standard CH₃NH₃PbI₃ precursor.[28] In the DSSC research community, alternative binary oxides such as ZnO,[29−32] SnO₂,[33,34] and Nb₂O₅[35−37] and ternary oxides such as SrTiO₃ (STO),[38−41] BaSnO₃,[42] and Zn₂SnO₄[43,44] have been explored as the electron transporter. For the perovskite photovoltaic research, only ZnO has been investigated as an alternative electron transporting layer so far,[13] and there is an urgent need
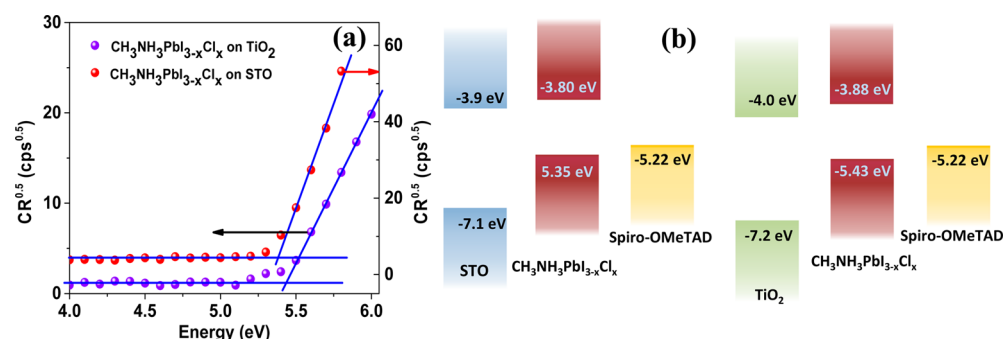
Figure 1. (a) Photoelectron emission spectroscopy in air to measure the ionization energies of the $CH_3NH_3PbI_{3-x}Cl_x$ layers on *meso*-STO and *meso*-TiO$_2$. (b) Schematics of band alignments between the electron-transporting STO (TiO$_2$), the perovskite $CH_3NH_3PbI_{3-x}Cl_x$, and the hole-transporting spiro-OMeTAD.

to explore wide band gap oxides with suitable band alignments and crystal structures to improve device performance, particularly V_{OC}.

The perovskite-structured oxide STO is well-known for its rich physical properties such as superconductivity,[45] ferroelectricity,[46] and thermoelectricity.[47] Recently, STO has also been used for photoassisted water splitting.[48,49] STO has a wide band gap similar to that of TiO$_2$, but its conduction band edge is slightly higher, matching better with the band structure of $CH_3NH_3PbI_{3-x}Cl_x$, which is beneficial for collecting photo-generated electrons. Notably, the room-temperature electron mobility of bulk STO is ~5–8 cm^2 V s^{-1},[50] which is much higher than that of TiO$_2$ (0.1–4 cm^2 V s^{-1}).[30] In addition, STO has a very high dielectric constant,[51] which helps to reduce charge recombination at the interface and subsequently improve device performance.

In this article, we report the first use of *meso*-STO as the electron-transporting layer in $CH_3NH_3PbI_{3-x}Cl_x$ solar cells, which boosts V_{OC} by ~120 mV and improves the fill factor (FF) compared to the *meso*-TiO$_2$ counterpart. We found that a $V_{OC} > 1$ V can be reliably achieved by increasing the *meso*-STO layer thickness, which is, however, accompanied by a decrease in photocurrent. Because the increase in V_{OC} is more than the difference in the conduction band edge between STO and TiO$_2$, we attribute the improvement in device performance to the better morphology of the $CH_3NH_3PbI_{3-x}Cl_x$ layer on *meso*-STO. Photoluminescence (PL) quenching and transient absorption spectra show efficient photoelectron transfer from $CH_3NH_3PbI_{3-x}Cl_x$ to *meso*-STO. Further optimizations of the *meso*-STO layer, particularly particle size, are expected to improve J_{SC} and hence efficiency.

2. EXPERIMENTAL SECTION

Materials Preparation. Methylammonium iodide (CH_3NH_3I) was synthesized following the previously reported method.[5,52] CH_3NH_3I and $PbCl_2$ were dissolved in anhydrous *N,N*-dimethylformamide at 3:1 molar ratio to produce a mixed halide perovskite precursor solution (40 wt %). Proper care should be taken when dealing with hazardous lead-containing compounds. STO paste was prepared using commercially available STO nanoparticles (Sigma-Aldrich, product no. 517011; average diameter ≤ 100 nm), and the procedure was similar to that in a previous report on preparing TiO$_2$ paste.[53] First, STO nanoparticles were dispersed in ethanol followed by adding ethyl cellulose, lauric acid, and terpineol, and then ethanol was removed from the solution using a rotary evaporator to obtain viscous pastes. Finally the paste was

diluted with ethanol in different weight ratios for the spin-coating. Commercially available TiO$_2$ paste (Dyesol DSL 18NR-T) was diluted in isopropyl alcohol to prepare the solution for *meso*-TiO$_2$.

Solar Cell Fabrication. Fluorine-doped tin oxide (F:SnO$_2$) coated glass (Pilkington TEC A7) was etched with Zn powder and 2 M HCl and then washed in deionized (DI) water. The etched substrate was then cleaned by detergent, DI water, acetone, and ethanol using ultrasonic cleaner, and then dried. The substrate underwent an oxygen plasma treatment for 10 min prior to the deposition of compact TiO$_2$ hole-blocking layer. Compact TiO$_2$ layer was deposited by spin-coating a mildly acetic solution of Ti-isopropoxide for 30 s at 2000 rpm. Then the coated thin film was dried at 150 °C for 15 min followed by an annealing at 450 °C for 30 min. We should note here that compact TiO$_2$ layers were used in all devices, and at present it remains a challenge to prepare STO compact layers with good hole-blocking properties. The *meso*-STO and *meso*-TiO$_2$ were deposited by spin-coating their respective diluted paste for 45 s with different rotation speeds and then annealed at 500 °C for 1 h. The perovskite precursor solution was then spin-coated on each prepared meso-electrode at 2000 rpm for 60 s and dried at 100 °C for ~1 h. A 68 mM spiro-OMeTAD solution in chlorobenzene containing 55 mM *tert*-butylpyridine and 9 mM lithium bis(trifluoromethylsyfonyl)imide salt was spun on the perovskite-coated substrate at a rate of 2000 rpm for 45 s, and then the cells were kept in the dark overnight. Finally about 100 nm Au electrode was evaporated by thermal evaporation to complete the device.

Materials Characterizations. The structure and morphology of the $CH_3NH_3PbI_{3-x}Cl_x$ grown on *meso*-STO and *meso*-TiO$_2$ films were examined by X-ray diffractometer (Bruker D8) and field emission scanning electron microscopy (FESEM, FEI Quanta 600FEG). The porosity and surface area of the mesoporous layers are measured using the Brunauer–Emmett–Teller (BET) method on a Micromeritics ASAP 2420 System. The ionization energy of $CH_3NH_3PbI_{3-x}Cl_x$ on *meso*-STO and TiO$_2$ was measured by photoelectron emission spectroscopy using Riken-AC2 photoelectron spectrometer. The optical properties of the device were measured before the deposition of the spiro-OMeTAD layer. The absorption spectra were measured using Varian carry 6000i spectrophotometer. The transmission spectra of *meso*-STO/TiO$_2$–compact TiO$_2$–FTO coated glass was measured by keeping air as the reference; on the other hand, the absorption spectra of the $CH_3NH_3PbI_{3-x}Cl_x$ on different meso-layers was measured by keeping the previous spectra as the reference. Photolumines-
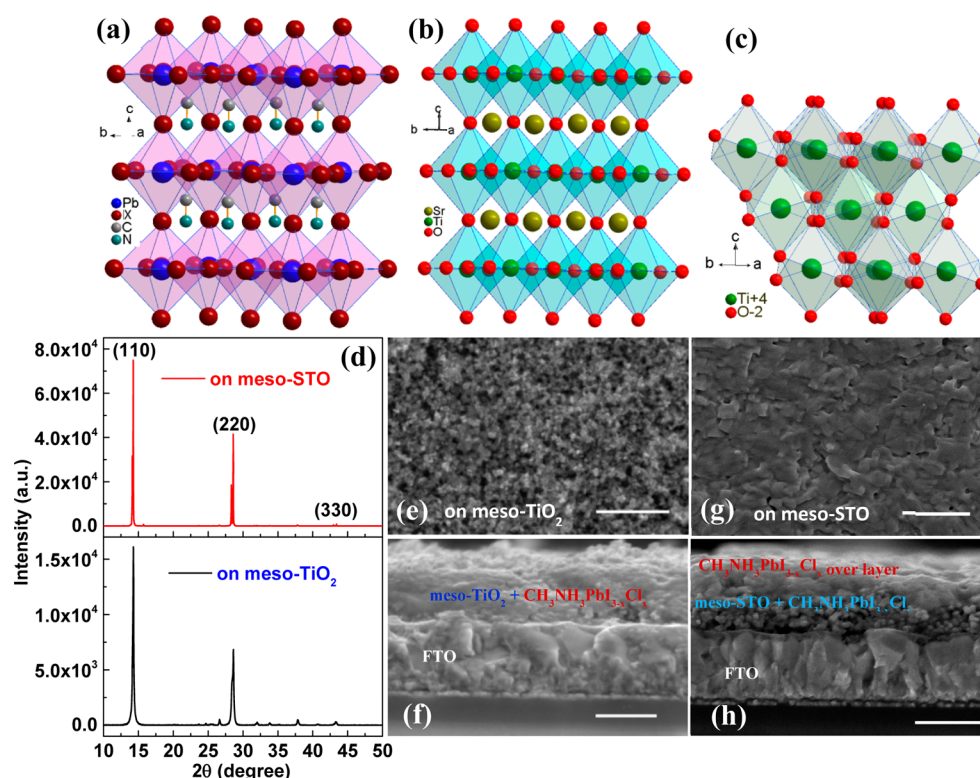
Figure 2. Crystal structures of (a) $CH_3NH_3PbX_3$ (X = I/Cl), (b) $SrTiO_3$, and (c) TiO_2. (d) X-ray diffraction patterns of $CH_3NH_3PbI_{3-x}Cl_x$ grown on *meso*-STO (top panel) and *meso*-TiO_2 (lower panel) layers. SEM images of $CH_3NH_3PbI_{3-x}Cl_x$ on *meso*-TiO_2: (e) top view and (f) cross-sectional view. SEM images of $CH_3NH_3PbI_{3-x}Cl_x$ on *meso*-STO: (g) top view and (h) cross-sectional view. The scale bars are 500 nm in all images.

cence spectra were measured by a Horiba Armis Raman setup, and the sample was illuminated using a visible laser of wavelength 632.81 nm. The thicknesses of the mesoporous STO layers were measured using Dektak 150 surface profiler.

Solar Cell Characterizations. The current density−voltage (*J*−*V*) curves were measured using Oriel PVIV test solution software connected with a source meter (Keithley 2400) under the illumination at 100 mW/cm² (AM 1.5G) from a solar simulator (Newport, Oriel Class A, 91195A) and a calibrated Si-reference cell certificated by NREL. The *J*−*V* curves of all devices were measured by masking the unwanted area with black tape so the exposed active area was 0.1 cm². The external quantum efficiency of the device was measured by Oriel IQE-200 quantum efficiency measurement system.

3. RESULTS AND DISCUSSION

Alignment between the conduction bands at the perovskite/oxide interface governs the extraction of photoelectrons, and the energetics of perovskite layers may depend on the different oxides used as the ETLs. Figure 1a shows the photoemission yield spectra in air for $CH_3NH_3PbI_{3-x}Cl_x$ layers on *meso*-STO and *meso*-TiO_2. The measured ionization energy of $CH_3NH_3PbI_{3-x}Cl_x$ on TiO_2 is −5.43 eV, consistent with the result measured by ultraviolet photoelectron spectroscopy.[54] Assuming a band gap of 1.55 eV,[12,55,56] the electron affinity of perovskite is estimated as −3.88 eV. These values are in good agreement with the ones commonly cited in the literature.[12,26,55] On the other hand, the valence band and the conduction band edges of $CH_3NH_3PbI_{3-x}Cl_x$ on STO were calculated to be −5.35 and −3.80 eV, respectively. These values are slightly higher than in the TiO_2 case. The schematic band alignment of the perovskite $CH_3NH_3PbI_{3-x}Cl_x$ with the

electron-transporting STO (TiO_2) and the HTL are illustrated in Figure 1b. The conduction band offset between $CH_3NH_3PbI_{3-x}Cl_x$ and STO (100 meV) is slightly lower than that between $CH_3NH_3PbI_{3-x}Cl_x$ and TiO_2 (120 meV), which is beneficial for increasing V_{OC} in solar cells. However, compact TiO_2 layers (40 nm) were used in all the devices; thus, the difference in the electron affinities in STO and TiO_2 should not be taken as the only factor dictating the value of V_{OC}. Nevertheless, the energetics of the perovskite/STO interface appears to be promising for achieving high solar cell performance.

The crystal structures of $CH_3NH_3PbX_3$, $SrTiO_3$, and TiO_2 are given in parts a, b, and c of Figure 2, respectively. In contrast to anatase TiO_2, both STO and $CH_3NH_3PbX_3$ have the ABX_3 perovskite structure. For cubic STO, A = Sr, B = Ti, and X = O, with alternative stacking of SrO and TiO_2 layers and lattice parameter *a* = 3.909 Å. For tetragonal $CH_3NH_3PbX_3$, A = (CH_3NH_3), B = Pb, and X = I or a mixture of I and Cl, with alternative stacking of CH_3NH_3X and PbX_2 layers, and the lattice parameters are *a* = 8.849 Å and *c* = 12.364 Å, as given in the literature.[18]

Figure 2d shows the X-ray diffraction (XRD) patterns for $CH_3NH_3PbI_{3-x}Cl_x$ grown on *meso*-STO and TiO_2 layers. The peaks at 14.2°, 28.6°, and 46.3° can be assigned to the (110), (220), and (330) planes of $CH_3NH_3PbI_{3-x}Cl_x$,[5,57] respectively. With a similar deposition condition of $CH_3NH_3PbI_{3-x}Cl_x$, the intensities of the three peaks are ∼5 times stronger for the sample grown on *meso*-STO than those on *meso*-TiO_2, which reveals the presence of a thick perovskite overlayer on *meso*-STO. Furthermore, we calculated the grain size of the $CH_3NH_3PbI_{3-x}Cl_x$ film grown on the meso layers using Scherrer's formula, $d = (0.94\lambda/(\beta \cos \theta))$, where λ is the Cu

$k_{\alpha 1}$ wavelength (0.1540598 nm), β is the full width at half-maximum (fwhm) of the peak, and θ is the Bragg angle. The estimated average grain sizes of the perovskites are about 230 and 65 nm for *meso*-STO and *meso*-TiO$_2$, respectively, and formation of larger grains on *meso*-STO indicates a higher crystalline quality.

Figure 2e−h shows the FESEM images of CH$_3$NH$_3$PbI$_{3-x}$Cl$_x$ on *meso*-TiO$_2$ and *meso*-STO layers. Both the top view in Figure 2e and the cross-sectional view in Figure 2f of CH$_3$NH$_3$PbI$_{3-x}$Cl$_x$ on *meso*-TiO$_2$ show the typical structure of mesopores infiltrated with perovskite. In contrast, the low surface area and total pore volume of *meso*-STO layers restrict the intake of CH$_3$NH$_3$PbI$_{3-x}$Cl$_x$ into the *meso*-STO layer. Besides penetrating into the mesopores, substantial CH$_3$NH$_3$PbI$_{3-x}$Cl$_x$ grows as a granular overlayer on the *meso*-STO with full surface coverage as shown in Figure 2g and h. Similar morphological differences of the spin-coated CH$_3$NH$_3$PbI$_{3-x}$Cl$_x$ films on *meso*-STO and *meso*-TiO$_2$ were also observed in samples with varied thicknesses (Figures S1 and S2, Supporting Information). These structural characteristics of spin-coated CH$_3$NH$_3$PbI$_{3-x}$Cl$_x$ films on *meso*-STO, particularly the full surface coverage with large and uniform grains, are expected to benefit the solar cell performance. However, at the same time, the low surface area and pore volume of *meso*-STO layers (due to larger particle sizes) inhibits the effective loading of perovskite into the pores of *meso*-STO, and the low perovskite/STO interfacial area limits the electron transfer. Considering this trade-off, we carefully optimized the thickness of the *meso*-STO layer to achieve the optimal solar cell performance, and we focus here on the devices with *meso*-STO layer thicknesses of 200 and 350 nm.

To study the compatibility and efficiency of STO as an ETL, we investigated the PL quenching of CH$_3$NH$_3$PbI$_{3-x}$Cl$_x$ emission by comparing the signals from both sides of the samples. PL quenching experiments are often used to explore the efficiency of charge transfer between the perovskite and the ETL/HTL because the charge transfer reduces the number of radiative recombination events. The PL spectra of CH$_3$NH$_3$PbI$_{3-x}$Cl$_x$ in Figure 3a show strong emission that peaks at a wavelength of ~765 nm, which corresponds to the band-edge emission.[17] On the other hand, by measuring from the other side of the samples with the oxide quencher, we found that the PL intensity of the perovskite significantly decreases in both *meso*-STO and *meso*-TiO$_2$ samples. We also measured the steady-state transmittance properties of the CH$_3$NH$_3$PbI$_{3-x}$Cl$_x$, and the spectra are given in Figure 3b. Compared to the TiO$_2$ case, CH$_3$NH$_3$PbI$_{3-x}$Cl$_x$ on *meso*-STO absorbs more light at wavelengths higher than 530 nm, while its absorption is lower at shorter wavelengths. Despite the higher optical absorbance at the excitation wavelength (633 nm), CH$_3$NH$_3$PbI$_{3-x}$Cl$_x$ grown on *meso*-STO exhibits lower PL intensity compared to that on *meso*-TiO$_2$, indicating efficient photoelectron transfer from CH$_3$NH$_3$PbI$_{3-x}$Cl$_x$ to STO. Besides the charge transfer efficiency, the difference in the PL quenching shown in Figure 3a may also originate from factors such as the difference in the morphology and the optical transmittance properties of the oxide mesoporous layers (Figure 3b). Because of the different morphologies of *meso*-STO and *meso*-TiO$_2$ (Figure S3 in Supporting Information), we cannot quantitatively ascribe the quenching efficiency as an intrinsic property of the perovskite/ETL interfaces. Nevertheless, the effective quenching of the CH$_3$NH$_3$PbI$_{3-x}$Cl$_x$ PL by the *meso*-STO indicates that *meso*-STO is a promising ETL in perovskite solar cells with the same architecture.

The schematics of the perovskite solar cells with *meso*-TiO$_2$ and *meso*-STO electron transporting layers are given in parts a and b of Figure 4, respectively. The average current density vs voltage (J−V) curves for a batch of 24 solar cells based on *meso*-TiO$_2$ and *meso*-STO are shown in Figure 4c, and their characteristic parameters are given in Table 1. Under one sun illumination of AM 1.5G, the *meso*-TiO$_2$ cell exhibits an average V_{OC} of 0.810 V, short circuit current (J_{SC}) of 16.76 mA/cm^2, and FF of 0.53, corresponding to an energy conversion efficiency η of 7.2%, which is comparable to the recently reported values in *meso*-TiO$_2$-based mixed-halide perovskite solar cells prepared by one-step spin-coating.[5,15,22,23,58] For the *meso*-STO-based devices, the average V_{OC} is 0.932 V and J_{SC} is 13.37 mA/cm^2, with FF of 0.56, leading to η of 6.97%. Our best-performing mp-STO-based cell produces J_{SC} of 14.85 mA/cm^2 and V_{OC} of 0.932 V, with FF of 0.55 and η of 7.55%. Its power conversion efficiency is slightly lower than that of the best-performing TiO$_2$-based cell (7.80%). The statistics of 24 devices made in the same batches for *meso*-STO and *meso*-TiO$_2$ are shown in the Supporting Information, Figures S4−S6.

The average V_{OC} of the *meso*-STO-based solar cells is ~15% higher than that of the *meso*-TiO$_2$-based ones. If the thickness in *meso*-STO layers is increased to 350 nm, V_{OC} can be further enhanced to 1.01 V. We also observed a notable increase of ~17% in the FF for the devices with thicker *meso*-STO as the ETL. These devices have very high shunt resistance of 2.5×10^4 Ω, which is about 3 times higher than that of *meso*-TiO$_2$ devices (8.1×10^3 Ω). The better surface coverage of the perovskite on *meso*-STO is most likely the origin of high shunt resistance as well as the improvements in V_{OC} and FF. However, as shown in Table 1, *meso*-STO-based solar cells generally suffer from low photocurrent compared to the TiO$_2$-based ones. With the increase of *meso*-STO thickness from 200 to 350 nm, the average J_{SC} decreases from 13.36 to 7.95 mA/cm^2, indicating less efficient carrier collection in devices with thicker STO layers. Although the FF is higher in the device with 350 nm *meso*-STO layers, the series resistance increases to 33 Ω, which is higher than that of 200 nm STO (19 Ω), causing a significant decrease of photocurrent for the devices with thick *meso*-STO ETLs.
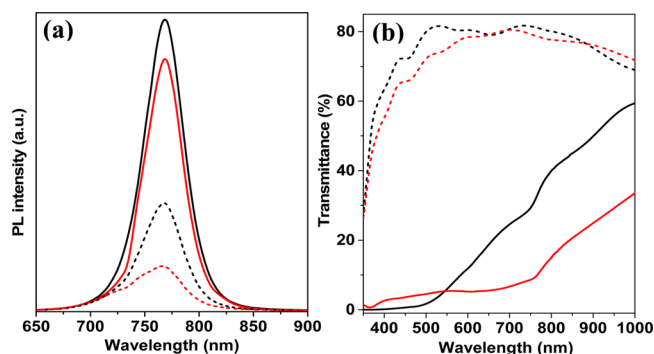
Figure 3. (a) PL spectra of CH$_3$NH$_3$PbI$_{3-x}$Cl$_x$ deposited on *meso*-TiO$_2$ (solid black line) and *meso*-STO (solid red line) measured from the perovskite side. Quenching of PL of CH$_3$NH$_3$PbI$_{3-x}$Cl$_x$ deposited on *meso*-TiO$_2$ (black dots) and *meso*-STO (red dots) measured from the oxide side. (b) Steady-state transmittance spectra of the CH$_3$NH$_3$PbI$_{3-x}$Cl$_x$ grown on either *meso*-TiO$_2$ (black line) or *meso*-STO (red line). The spectra of the uncoated *meso*-TiO$_2$ (black dots) and *meso*-STO (red dots) are also shown.
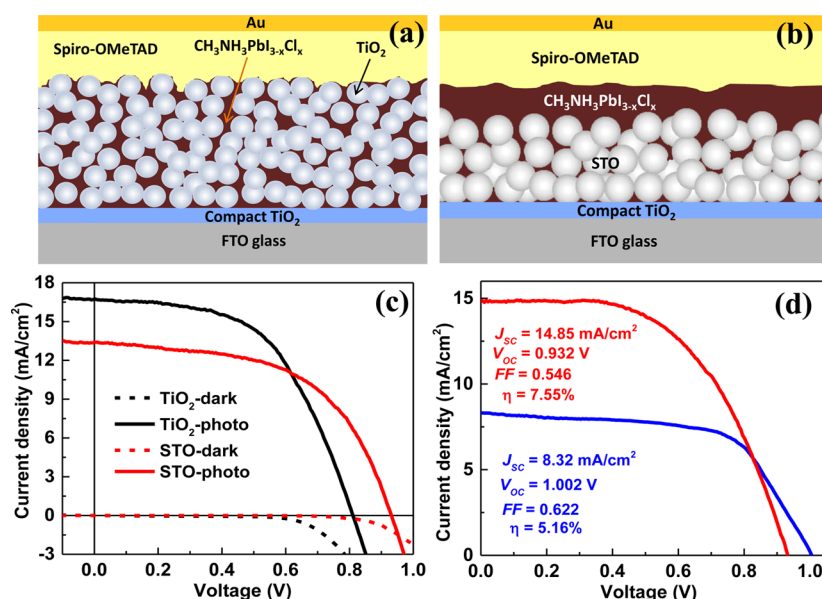
Figure 4. Schematic of the $CH_3NH_3PbI_{3-x}Cl_x$ solar cells with (a) *meso*-TiO$_2$ and (b) *meso*-STO as electron-transporting materials. (c) Average $J-V$ characteristics of a batch of 24 devices using *meso*-TiO$_2$ and *meso*-STO. (d) $J-V$ characteristics of two typical solar cells with the *meso*-STO thicknesses of 200 nm (red) and 350 nm (blue).

Table 1. Photovoltaic Parameters Derived from the $J-V$ Characteristics for $CH_3NH_3PbI_{3-x}Cl_x$ Solar Cells Using Either *meso*-STO or *meso*-TiO$_2$

sample (thickness)	J_{SC} (mA/cm^2) (max)	V_{OC} (V) (max)	FF (max)	η % (max)
meso-STO (200 nm)	13.37 ± 1.78	0.93 ± 0.05	0.56 ± 0.06	6.97 ± 2.08
meso-STO (350 nm)	7.95 ± 1.53	1.00 ± 0.05	0.62 ± 0.04	4.23 ± 1.53
meso-TiO$_2$ (550 nm)	16.76 ± 1.86	0.81 ± 0.07	0.53 ± 0.06	7.19 ± 2.26

The external quantum efficiency (EQE) of STO and TiO$_2$-based $CH_3NH_3PbI_{3-x}Cl_x$ solar cells was measured by monitoring the photocurrent at different wavelengths, and the data are shown in Figure 5. Compared to the TiO$_2$-based
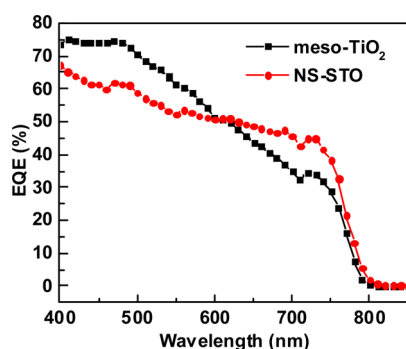
**Figure 5.** EQE spectra of the solar cells using either *meso*-TiO$_2$ or *meso*-STO as the electron-transporting layers.

device, the EQE of the STO-based device is higher in the long-wavelength region (>600 nm) of the solar spectrum but is lower in the short-wavelength region (<600 nm). However, we should note that this difference in the wavelength dependence is related to the variation in the transmittance of the *meso*-oxide ETLs because the short-wavelength transmittance of STO appears to be weaker than that of TiO$_2$ (Figure 3b). Nevertheless, as shown in Figure 5, the perovskite device with *meso*-STO exhibits better performance in converting long-

wavelength photons into carriers compared to the TiO$_2$ counterpart.

Because transient absorption (TA) spectroscopy provides direct information regarding carrier dynamics and excited-state deactivation pathways, including electron injection, we utilized this method to probe the events that occur upon photo-excitation of $CH_3NH_3PbI_{3-x}Cl_x$ with STO and TiO$_2$. The experimental setup was detailed elsewhere.[59] A white-light continuum that was generated by a super continuum source was used as probe pulses. The pump pulses at 440 nm were created from femtosecond pulses generated in an optical parametric amplifier (Spectra-Physics). The pump and probe beams were focused on the sample, and the transmitted probe light from the samples was collected and focused on the broadband UV−visible detector to record time-resolved transient absorption spectra. As shown in Figure 6, the recovery of the negative signal observed at ~765 nm, which is attributed to the stimulated emission and ground-state bleach of the perovskite,[17,60] is slightly faster in the bilayers of $CH_3NH_3PbI_{3-x}Cl_x$ with STO than in the TiO$_2$ case. Notably, the negative peak intensity is decreased for $CH_3NH_3PbI_{3-x}Cl_x$−STO compared with $CH_3NH_3PbI_{3-x}Cl_x$−TiO$_2$, which is also in good agreement with the steady-state PL results (Figure 3a).

Because the transient optical measurement revealed very efficient charge transfer at the STO/perovskite interface, the decrease of photocurrent in the solar cells with STO as the ETL most likely originates from the structural differences between the two meso-structures. It is well-known that the morphology of mesoporous ETL is important for the loading and
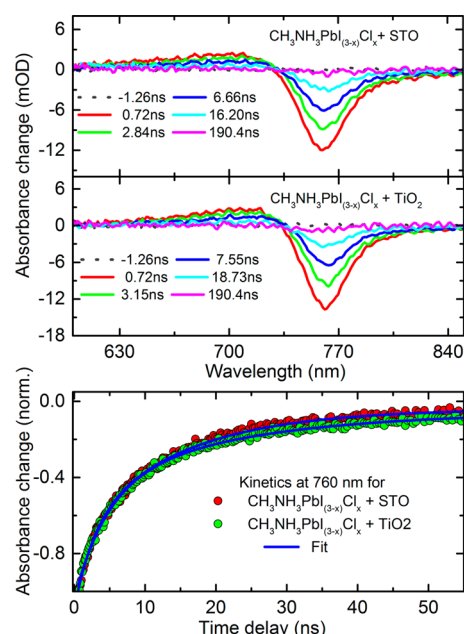
Figure 6. Transient absorption spectra of the thin film bilayers of $CH_3NH_3PbI_{3-x}Cl_x$ with STO and TiO_2 (top panel). The lower panel shows the normalized time profile of transient absorption for $CH_3NH_3PbI_{3-x}Cl_x$ with STO (red dots) and with TiO_2 (green dots) measured at 440 nm excitation (1 kHz, 35 fs, 4.5 μJ/cm^2) with a characteristic time constant of 2.7 and 3.1 ns, respectively, which is consistent with the literature.[9,61]

performance of perovskites in the solar cells. From the BET measurements of the mesoporous electrodes, we estimated the values of average pore diameter and surface area (Table ST1, Supporting Information). The average pore size and surface area of *meso*-TiO_2 are 23.66 nm and 69 m^2/g, respectively, which are similar to the values reported previously.[62] On the other hand, the average pore size of *meso*-STO is 45.27 nm, which is a result of the larger size of STO nanoparticles (~70 nm) compared to that of TiO_2 nanoparticles (~20 nm). The surface area of *meso*-STO is 24 m^2/g, which is almost 3 times smaller than that of TiO_2. The morphology of *meso*-STO reduces the overall interfacial areas between the perovskite and the ETL, limiting the overall charge collection. It has been reported for dye-sensitized solar cells that the recombination lifetime of the charge carriers and the charge injection efficiency drop significantly with increasing TiO_2 particle size.[63−65] Improving the morphology of *meso*-STO, particularly optimizing the STO particle size, is clearly needed for increasing the photocurrent and the efficiency.

There are multiple factors concurrently contributing to the value of V_{OC}. In a single heterojunction solar cell,

$$V_{OC} = \frac{nkT}{q} \ln\left(\frac{J_{SC}}{J_0} + 1\right) \tag{1}$$

where n is the diode ideality factors, k is the Boltzmann constant, T is the temperature, and J_0 is the reverse saturated current density. The higher V_{OC} in solar cells with *meso*-STO is consistent with the lower darker current as shown in Figure 4c. In organic solar cells, V_{OC} is related to the difference between E^A_{LUMO} and E^D_{HOMO}.[66] In hybrid materials like halide perovskites, the higher conduction band edge of STO and the smaller band edge offset as shown in Figure 1 are beneficial

for increasing V_{OC}. Furthermore, as V_{OC} is the voltage at which the total current is zero, it depends fundamentally on the balance between the charge carrier generation and recombination in the active regions.[67] For DSSC, the undesired direct recombination of electrons in mesoporous ETL with holes in HTL has significant effects on V_{OC}.[20] In the perovskite solar cells with *meso*-STO, the presence of the uniform perovskite overlayer eliminates the direct contact between ETL and spiro-MeOTAD, and hence the reduced recombination of photogenerated carriers is expected to lead to improvements in V_{OC} and FF.

4. CONCLUSIONS

In summary, we have demonstrated enhanced open circuit voltage and fill factor with the use of perovskite oxide STO as a new electron-transporting layer in mixed-halide hybrid perovskite solar cells. With a one-step spin-coating process, we have achieved an open circuit voltage of 1.01 V in such STO-based devices, which is ~25% higher than the value of 0.81 V for the devices with the conventional mesoscopic TiO_2. Favorable band alignment along with improved surface coverage of the perovskite layer on *meso*-STO contributes to the performance of solar cells with STO as the electron-transporting layer. Our transient absorption (TA) spectroscopy experiments also revealed that the photoelectron transfer rate is slightly higher from $CH_3NH_3PbI_{3-x}Cl_x$ to STO compared to that from $CH_3NH_3PbI_{3-x}Cl_x$ to TiO_2. On the other hand, reduced overall surface area of the *meso*-STO due to the large particle size compromises the photocurrent, which requires further improvement of the *meso*-STO layers. Overall, our results underscore STO as a promising electron-transporting material for further unleashing the high-performance potential of hybrid mixed-halide perovskite solar cells.

■ ASSOCIATED CONTENT

Ⓢ Supporting Information

SEM images of the $CH_3NH_3PbI_{3-x}Cl_x$ and the mesoporous layers, optical transmittance, gas absorption and BET of the mesoporous layers, and statistics of device performance. This material is available free of charge via the Internet at http://pubs.acs.org.

■ AUTHOR INFORMATION

Corresponding Authors
*E-mail: omar.abdelsaboor@kaust.edu.sa.
*E-mail: tao.wu@kaust.edu.sa.

Notes
The authors declare no competing financial interest.

■ REFERENCES

(1) Kamat, P. V. Evolution of Perovskite Photovoltaics and Decrease in Energy Payback Time. *J. Phys. Chem. Lett.* **2013**, *4*, 3733−3734.

(2) Burschka, J.; Pellet, N.; Moon, S.-J.; Humphry-Baker, R.; Gao, P.; Nazeeruddin, M. K.; Graetzel, M. Sequential Deposition as a Route to High-Performance Perovskite-Sensitized Solar Cells. *Nature* **2013**, *499*, 316−319.

(3) Docampo, P.; Ball, J. M.; Darwich, M.; Eperon, G. E.; Snaith, H. J. Efficient Organometal Trihalide Perovskite Planar-Heterojunction

28499

dx.doi.org/10.1021/jp509753p | *J. Phys. Chem. C* 2014, 118, 28494−28501

Solar Cells on Flexible Polymer Substrates. *Nat. Commun.* **2013**, *4*, 2761.

(4) Heo, J. H.; Im, S. H.; Noh, J. H.; Mandal, T. N.; Lim, C.-S.; Chang, J. A.; Lee, Y. H.; Kim, H.-j.; Sarkar, A.; Nazeeruddin, M. K.; Graetzel, M.; Seok, S. I. Efficient Inorganic−Organic Hybrid Heterojunction Solar Cells Containing Perovskite Compound and Polymeric Hole Conductors. *Nat. Photonics* **2013**, *7*, 487−492.

(5) Lee, M. M.; Teuscher, J.; Miyasaka, T.; Murakami, T. N.; Snaith, H. J. Efficient Hybrid Solar Cells Based on Meso-Superstructured Organometal Halide Perovskites. *Science* **2012**, *338*, 643−647.

(6) Leijtens, T.; Eperon, G. E.; Pathak, S.; Abate, A.; Lee, M. M.; Snaith, H. J. Overcoming Ultraviolet Light Instability of Sensitized TiO$_2$ with Meso-Superstructured Organometal Tri-halide Perovskite Solar Cells. *Nat. Commun.* **2013**, *4*, 2885.

(7) Liu, M.; Johnston, M. B.; Snaith, H. J. Efficient planar heterojunction perovskite solar cells by vapour deposition. *Nature* **2013**, *501*, 395−398.

(8) Marchioro, A.; Teuscher, J.; Friedrich, D.; Kunst, M.; van de Krol, R.; Moehl, T.; Graetzel, M.; Moser, J.-E. Unravelling the Mechanism of Photoinduced Charge Transfer Processes in Lead iodide Perovskite Solar Cells. *Nat. Photonics* **2014**, *8*, 250−255.

(9) Stranks, S. D.; Eperon, G. E.; Grancini, G.; Menelaou, C.; Alcocer, M. J. P.; Leijtens, T.; Herz, L. M.; Petrozza, A.; Snaith, H. J. Electron-Hole Diffusion Lengths Exceeding 1 Micrometer in an Organometal Trihalide Perovskite Absorber. *Science* **2013**, *342*, 341−344.

(10) Xing, G.; Mathews, N.; Sun, S.; Lim, S. S.; Lam, Y. M.; Graetzel, M.; Mhaisalkar, S.; Sum, T. C. Long-Range Balanced Electron- and Hole-Transport Lengths in Organic−Inorganic CH$_3$NH$_3$PbI$_3$. *Science* **2013**, *342*, 344−347.

(11) Etgar, L.; Gao, P.; Xue, Z.; Peng, Q.; Chandiran, A. K.; Liu, B.; Nazeeruddin, M. K.; Graetzel, M. Mesoscopic CH$_3$NH$_3$PbI$_3$/TiO$_2$ Heterojunction Solar Cells. *J. Am. Chem. Soc.* **2012**, *134*, 17396−17399.

(12) Kim, H.-S.; Lee, C.-R.; Im, J.-H.; Lee, K.-B.; Moehl, T.; Marchioro, A.; Moon, S.-J.; Humphry-Baker, R.; Yum, J.-H.; Moser, J. E.; Graetzel, M.; Park, N.-G. Lead Iodide Perovskite Sensitized All-Solid-State Submicron Thin Film Mesoscopic Solar Cell with Efficiency Exceeding 9%. *Sci. Rep.* **2012**, *2*, 591.

(13) Liu, D.; Kelly, T. L. Perovskite Solar Cells with a Planar Heterojunction Structure Prepared Using Room-Temperature Solution Processing Techniques. *Nat. Photonics* **2014**, *8*, 133−138.

(14) Christians, J. A.; Fung, R. C. M.; Kamat, P. V. An Inorganic Hole Conductor for Organo-Lead Halide Perovskite Solar Cells. Improved Hole Conductivity with Copper Iodide. *J. Am. Chem. Soc.* **2014**, *136*, 758−764.

(15) Crossland, E. J.; Noel, N.; Sivaram, V.; Leijtens, T.; Alexander-Webber, J. A.; Snaith, H. J. Mesoporous TiO$_2$ Single Crystals Delivering Enhanced Mobility and Optoelectronic Device Performance. *Nature* **2013**, *495*, 215−219.

(16) Rong, Y.; Ku, Z.; Mei, A.; Liu, T.; Xu, M.; Ko, S.; Li, X.; Han, H. Hole-Conductor-Free Mesoscopic TiO$_2$/CH$_3$NH$_3$PbI$_3$ Heterojunction Solar Cells Based on Anatase Nanosheets and Carbon Counter Electrodes. *J. Phys. Chem. Lett.* **2014**, 2160−2164.

(17) Zhu, Z.; Ma, J.; Wang, Z.; Mu, C.; Fan, Z.; Du, L.; Bai, Y.; Fan, L.; Yan, H.; Phillips, D. L.; Yang, S. Efficiency Enhancement of Perovskite Solar Cells through Fast Electron Extraction: The Role of Graphene Quantum Dots. *J. Am. Chem. Soc.* **2014**, *136*, 3760−3763.

(18) Stoumpos, C. C.; Malliakas, C. D.; Kanatzidis, M. G. Semiconducting Tin and Lead Iodide Perovskites with Organic Cations: Phase Transitions, High Mobilities, and Near-Infrared Photoluminescent Properties. *Inorg. Chem.* **2013**, *52*, 9019−9038.

(19) Snaith, H. J. Perovskites: The Emergence of a New Era for Low-Cost, High-Efficiency Solar Cells. *J. Phys. Chem. Lett.* **2013**, *4*, 3623−3630.

(20) Boschloo, G.; Hagfeldt, A. Characteristics of the Iodide/Triiodide Redox Mediator in Dye-Sensitized Solar Cells. *Acc. Chem. Res.* **2009**, *42*, 1819−1826.

(21) Raga, S. R.; Barea, E. M.; Fabregat-Santiago, F. Analysis of the Origin of Open Circuit Voltage in Dye Solar Cells. *J. Phys. Chem. Lett.* **2012**, *3*, 1629−1634.

(22) Leijtens, T.; Lauber, B.; Eperon, G. E.; Stranks, S. D.; Snaith, H. J. The Importance of Perovskite Pore Filling in Organometal Mixed Halide Sensitized TiO$_2$-Based Solar Cells. *J. Phys. Chem. Lett.* **2014**, *5*, 1096−1102.

(23) Snaith, H. J.; Abate, A.; Ball, J. M.; Eperon, G. E.; Leijtens, T.; Noel, N. K.; Stranks, S. D.; Wang, J. T.-W.; Wojciechowski, K.; Zhang, W. Anomalous Hysteresis in Perovskite Solar Cells. *J. Phys. Chem. Lett.* **2014**, *5*, 1511−1515.

(24) Jeon, N. J.; Lee, J.; Noh, J. H.; Nazeeruddin, M. K.; Grätzel, M.; Seok, S. I. Efficient Inorganic−Organic Hybrid Perovskite Solar Cells Based on Pyrene Arylamine Derivatives as Hole-Transporting Materials. *J. Am. Chem. Soc.* **2013**, *135*, 19087−19090.

(25) Lee, J.-W.; Seol, D.-J.; Cho, A.-N.; Park, N.-G. High-Efficiency Perovskite Solar Cells Based on the Black Polymorph of HC-(NH$_2$)$_2$PbI$_3$. *Adv. Mater.* **2014**, *26*, 4991−4998.

(26) Ryu, S.; Noh, J. H.; Jeon, N. J.; Chan Kim, Y.; Yang, W. S.; Seo, J.; Seok, S. I. Voltage Output of Efficient Perovskite Solar Cells with High Open-Circuit Voltage and Fill Factor. *Energy Environ. Sci.* **2014**, *7*, 2614−2618.

(27) Qin, P.; Paek, S.; Dar, M. I.; Pellet, N.; Ko, J.; Grätzel, M.; Nazeeruddin, M. K. Perovskite Solar Cells with 12.8% Efficiency by Using Conjugated Quinolizino Acridine Based Hole Transporting Material. *J. Am. Chem. Soc.* **2014**, *136*, 8516−8519.

(28) Zhao, Y.; Zhu, K. CH$_3$NH$_3$Cl-Assisted One-Step Solution Growth of CH$_3$NH$_3$PbI$_3$: Structure, Charge-Carrier Dynamics, and Photovoltaic Properties of Perovskite Solar Cells. *J. Phys. Chem. C* **2014**, *118*, 9412−9418.

(29) Tiwana, P.; Docampo, P.; Johnston, M. B.; Snaith, H. J.; Herz, L. M. Electron Mobility and Injection Dynamics in Mesoporous ZnO, SnO$_2$, and TiO$_2$ Films Used in Dye-Sensitized Solar Cells. *ACS Nano* **2011**, *5*, 5158−5166.

(30) Zhang, Q.; Dandeneau, C. S.; Zhou, X.; Cao, G. ZnO Nanostructures for Dye-Sensitized Solar Cells. *Adv. Mater.* **2009**, *21*, 4087−4108.

(31) Martinson, A. B. F.; Elam, J. W.; Hupp, J. T.; Pellin, M. J. ZnO Nanotube Based Dye-Sensitized Solar Cells. *Nano Lett.* **2007**, *7*, 2183−2187.

(32) Zhu, X.; Nepomnyashchii, A. B.; Roitberg, A. E.; Parkinson, B. A.; Schanze, K. S. Photosensitization of Single-Crystal ZnO by a Conjugated Polyelectrolyte Designed to Avoid Aggregation. *J. Phys. Chem. Lett.* **2013**, *4*, 3216−3220.

(33) Snaith, H. J.; Ducati, C. SnO$_2$-Based Dye-Sensitized Hybrid Solar Cells Exhibiting Near Unity Absorbed Photon-to-Electron Conversion Efficiency. *Nano Lett.* **2010**, *10*, 1259−1265.

(34) Ferrere, S.; Zaban, A.; Gregg, B. A. Dye Sensitization of Nanocrystalline Tin Oxide by Perylene Derivatives. *J. Phys. Chem. B* **1997**, *101*, 4490−4493.

(35) Le Viet, A.; Jose, R.; Reddy, M. V.; Chowdari, B. V. R.; Ramakrishna, S. Nb$_2$O$_5$ Photoelectrodes for Dye-Sensitized Solar Cells: Choice of the Polymorph. *J. Phys. Chem. C* **2010**, *114*, 21795−21800.

(36) Ghosh, R.; Brennaman, M. K.; Uher, T.; Ok, M.-R.; Samulski, E. T.; McNeil, L. E.; Meyer, T. J.; Lopez, R. Nanoforest Nb$_2$O$_5$ Photoanodes for Dye-Sensitized Solar Cells by Pulsed Laser Deposition. *ACS Appl. Mater. Interfaces* **2011**, *3*, 3929−3935.

(37) Ou, J. Z.; Rani, R. A.; Ham, M.-H.; Field, M. R.; Zhang, Y.; Zheng, H.; Reece, P.; Zhuiykov, S.; Sriram, S.; Bhaskaran, M.; et al. Elevated Temperature Anodized Nb$_2$O$_5$: A Photoanode Material with Exceptionally Large Photoconversion Efficiencies. *ACS Nano* **2012**, *6*, 4045−4053.

(38) Yang, S.; Kou, H.; Wang, J.; Xue, H.; Han, H. Tunability of the Band Energetics of Nanostructured SrTiO$_3$ Electrodes for Dye-Sensitized Solar Cells. *J. Phys. Chem. C* **2010**, *114*, 4245−4249.

(39) Dabestani, R.; Bard, A. J.; Campion, A.; Fox, M. A.; Mallouk, T. E.; Webber, S. E.; White, J. M. Sensitization of titanium dioxide and strontium titanate electrodes by ruthenium(II) tris(2,2′-bipyridine-

4,4′-dicarboxylic acid) and zinc tetrakis(4-carboxyphenyl)porphyrin: An evaluation of sensitization efficiency for component photoelectrodes in a multipanel device. *J. Phys. Chem.* **1988**, *92*, 1872−1878.

(40) Burnside, S.; Moser, J. E.; Brooks, K.; Gratzel, M.; Cahen, D. Nanocrystalline Mesoporous Strontium Titanate as Photoelectrode Material for Photosensitized Solar Devices: Increasing Photovoltage Through Flatband Potential Engineering. *J. Phys. Chem. B* **1999**, *103*, 9328−9332.

(41) Lan, J.-L.; Liang, Z.; Yang, Y.-H.; Ohuchi, F. S.; Jenekhe, S. A.; Cao, G. The Effect of $SrTiO_3$:ZnO as Cathodic Buffer Layer for Inverted Polymer Solar Cells. *Nano Energy* **2014**, *4*, 140−149.

(42) Shin, S. S.; Kim, J. S.; Suk, J. H.; Lee, K. D.; Kim, D. W.; Park, J. H.; Cho, I. S.; Hong, K. S.; Kim, J. Y. Improved Quantum Efficiency of Highly Efficient Perovskite $BaSnO_3$-Based Dye-Sensitized Solar Cells. *ACS Nano* **2013**, *7*, 1027−1035.

(43) Choi, S.-H.; Hwang, D.; Kim, D.-Y.; Kervella, Y.; Maldivi, P.; Jang, S.-Y.; Demadrille, R.; Kim, I.-D. Amorphous Zinc Stannate (Zn_2SnO_4) Nanofibers Networks as Photoelectrodes for Organic Dye-Sensitized Solar Cells. *Adv. Funct. Mater.* **2013**, *23*, 3146−3155.

(44) Tan, B.; Toman, E.; Li, Y.; Wu, Y. Zinc stannate (Zn_2SnO_4) dye-sensitized solar cells. *J. Am. Chem. Soc.* **2007**, *129*, 4162−4163.

(45) Ueno, K.; Nakamura, S.; Shimotani, H.; Ohtomo, A.; Kimura, N.; Nojima, T.; Aoki, H.; Iwasa, Y.; Kawasaki, M. Electric-Field-Induced Superconductivity in an Insulator. *Nat. Mater.* **2008**, *7*, 855−858.

(46) Dawber, M.; Rabe, K. M.; Scott, J. F. Physics of Thin-Film Ferroelectric Oxides. *Rev. Mod. Phys.* **2005**, *77*, 1083−1130.

(47) Ohta, H.; Kim, S.; Mune, Y.; Mizoguchi, T.; Nomura, K.; Ohta, S.; Nomura, T.; Nakanishi, Y.; Ikuhara, Y.; Hirano, M.; et al. Giant Thermoelectric Seebeck Coefficient of a Two-Dimensional Electron Gas in $SrTiO_3$. *Nat. Mater.* **2007**, *6*, 129−134.

(48) Arai, T.; Sato, S.; Kajino, T.; Morikawa, T. Solar CO_2 Reduction Using H_2O by a Semiconductor/Metal-Complex Hybrid Photocatalyst: Enhanced Efficiency and Demonstration of a Wireless System Using $SrTiO_3$ Photoanodes. *Energy Environ. Sci.* **2013**, *6*, 1274−1282.

(49) Ouyang, S.; Tong, H.; Umezawa, N.; Cao, J.; Li, P.; Bi, Y.; Zhang, Y.; Ye, J. Surface-Alkalinization-Induced Enhancement of Photocatalytic H_2 Evolution Over $SrTiO_3$-Based Photocatalysts. *J. Am. Chem. Soc.* **2012**, *134*, 1974−1977.

(50) Tufte, O. N.; Chapman, P. W. Electron Mobility in Semiconducting Strontium Titanate. *Phys. Rev.* **1967**, *155*, 796−802.

(51) Müller, K. A.; Burkard, H. $SrTiO_3$: An Intrinsic Quantum Paraelectric Below 4 K. *Phys. Rev. B* **1979**, *19*, 3593−3602.

(52) Wu, K.; Bera, A.; Ma, C.; Du, Y.; Yang, Y.; Li, L.; Wu, T. T. Temperature-Dependent Excitonic Photoluminescence of Hybrid Organometal Halide Perovskite Films. *Phys. Chem. Chem. Phys.* **2014**, *16*, 22476−22481.

(53) Kim, M.-J.; Lee, C.-R.; Jeong, W.-S.; Im, J.-H.; Ryu, T. I.; Park, N.-G. Unusual Enhancement of Photocurrent by Incorporation of Brönsted Base Thiourea into Electrolyte of Dye-Sensitized Solar Cell. *J. Phys. Chem. C* **2010**, *114*, 19849−19852.

(54) Schulz, P.; Edri, E.; Kirmayer, S.; Hodes, G.; Cahen, D.; Kahn, A. Interface Energetics in Organo-Metal Halide Perovskite-Based Photovoltaic Cells. *Energy Environ. Sci.* **2014**, *7*, 1377−1381.

(55) Qin, P.; Tanaka, S.; Ito, S.; Tetreault, N.; Manabe, K.; Nishino, H.; Nazeeruddin, M. K.; Grätzel, M. Inorganic Hole Conductor-Based Lead Halide Perovskite Solar Cells with 12.4% Conversion Efficiency. *Nat. Commun.* **2014**, *5*, 3834.

(56) Mei, A.; Li, X.; Liu, L.; Ku, Z.; Liu, T.; Rong, Y.; Xu, M.; Hu, M.; Chen, J.; Yang, Y.; et al. A Hole-Conductor−Free, Fully Printable Mesoscopic Perovskite Solar Cell With High Stability. *Science* **2014**, *345*, 295−298.

(57) Kojima, A.; Teshima, K.; Shirai, Y.; Miyasaka, T. Organometal Halide Perovskites as Visible-Light Sensitizers for Photovoltaic Cells. *J. Am. Chem. Soc.* **2009**, *131*, 6050−6051.

(58) Di Giacomo, F.; Razza, S.; Matteocci, F.; D'Epifanio, A.; Licoccia, S.; Brown, T. M.; Di Carlo, A. High Efficiency $CH_3NH_3PbI_{(3−x)}Cl_x$ Perovskite Solar Cells With Poly(3-hexylthiophene) Hole Transport Layer. *J. Power Sources* **2014**, *251*, 152−156.

(59) Mohammed, O. F.; Xiao, D.; Batista, V. S.; Nibbering, E. T. J. Excited-State Intramolecular Hydrogen Transfer (ESIHT) of 1,8-Dihydroxy-9,10-anthraquinone (DHAQ) Characterized by Ultrafast Electronic and Vibrational Spectroscopy and Computational Modeling. *J. Phys. Chem. A* **2014**, *118*, 3090−3099.

(60) Manser, J. S.; Kamat, P. V. Band filling with free charge carriers in organometal halide perovskites. *Nat. Photonics* **2014**, *8*, 737−743.

(61) Deschler, F.; Price, M.; Pathak, S.; Klintberg, L. E.; Jarausch, D.-D.; Higler, R.; Hüttner, S.; Leijtens, T.; Stranks, S. D.; Snaith, H. J.; et al. High Photoluminescence Efficiency and Optically Pumped Lasing in Solution-Processed Mixed Halide Perovskite Semiconductors. *J. Phys. Chem. Lett.* **2014**, *5*, 1421−1426.

(62) Samadpour, M.; Giménez, S.; Boix, P. P.; Shen, Q.; Calvo, M. E.; Taghavinia, N.; Iraji zad, A.; Toyoda, T.; Míguez, H.; Mora-Seró, I. Effect of Nanostructured Electrode Architecture and Semiconductor Deposition Strategy on the Photovoltaic Performance of Quantum Dot Sensitized Solar Cells. *Electrochim. Acta* **2012**, *75*, 139−147.

(63) Nakade, S.; Saito, Y.; Kubo, W.; Kitamura, T.; Wada, Y.; Yanagida, S. Influence of TiO_2 Nanoparticle Size on Electron Diffusion and Recombination in Dye-Sensitized TiO_2 Solar Cells. *J. Phys. Chem. B* **2003**, *107*, 8607−8611.

(64) Katoh, R.; Huijser, A.; Hara, K.; Savenije, T. J.; Siebbeles, L. D. A. Effect of the Particle Size on the Electron Injection Efficiency in Dye-Sensitized Nanocrystalline TiO_2 Films Studied by Time-Resolved Microwave Conductivity (TRMC) Measurements. *J. Phys. Chem. C* **2007**, *111*, 10741−10746.

(65) Jeng, M.-J.; Wung, Y.-L.; Chang, L.-B.; Chow, L. Particle Size Effects of TiO_2 Layers on the Solar Efficiency of Dye-Sensitized Solar Cells. *Int. J. Photoenergy* **2013**, *2013*, 563897.

(66) Janssen, R. A. J.; Nelson, J. Factors Limiting Device Efficiency in Organic Photovoltaics. *Adv. Mater.* **2013**, *25*, 1847−1858.

(67) Blakesley, J. C.; Neher, D. Relationship Between Energetic Disorder and Open-Circuit Voltage in Bulk Heterojunction Organic Solar Cells. *Phys. Rev. B* **2011**, *84*, 075210.